

CHEMO-hydrodynamic coupling between forced advection in porous media and self-sustained chemical waves

S. Atis, S. Saha, H. Auradou, J. Martin, N. Rakotomalala et al.

Citation: *Chaos* **22**, 037108 (2012); doi: 10.1063/1.4734489

View online: <http://dx.doi.org/10.1063/1.4734489>

View Table of Contents: <http://chaos.aip.org/resource/1/CHAOEH/v22/i3>

Published by the [American Institute of Physics](http://www.aip.org).

Related Articles

The heads and tails of buoyant autocatalytic balls

Chaos **22**, 037110 (2012)

Influence of temperature on linear stability in buoyancy-driven fingering of reaction-diffusion fronts

Chaos **22**, 037107 (2012)

Invariant manifolds and the geometry of front propagation in fluid flows

Chaos **22**, 037104 (2012)

Marangoni-driven convection around exothermic autocatalytic chemical fronts in free-surface solution layers

Chaos **22**, 037106 (2012)

Asymptotic structure of laminar diffusion flames at high pressure

Phys. Fluids **24**, 093602 (2012)

Additional information on Chaos

Journal Homepage: <http://chaos.aip.org/>

Journal Information: http://chaos.aip.org/about/about_the_journal

Top downloads: http://chaos.aip.org/features/most_downloaded

Information for Authors: <http://chaos.aip.org/authors>

ADVERTISEMENT



AIP Advances

Submit Now

**Explore AIP's new
open-access journal**

- **Article-level metrics
now available**
- **Join the conversation!
Rate & comment on articles**

CHEMO-hydrodynamic coupling between forced advection in porous media and self-sustained chemical waves

S. Atis, S. Saha, H. Auradou, J. Martin, N. Rakotomalala, L. Talon, and D. Salin
Laboratoire Fluides Automatique et Systèmes Thermiques, Universités P. et M. Curie and Paris Sud, C.N.R.S. (UMR7608), Bâtiment 502, Campus Universitaire, 91405 Orsay Cedex, France

(Received 15 April 2012; accepted 22 June 2012; published online 28 September 2012)

Autocatalytic reaction fronts between two reacting species in the absence of fluid flow, propagate as solitary waves. The coupling between autocatalytic reaction front and forced simple hydrodynamic flows leads to stationary fronts whose velocity and shape depend on the underlying flow field. We address the issue of the chemico-hydrodynamic coupling between forced advection in porous media and self-sustained chemical waves. Towards that purpose, we perform experiments over a wide range of flow velocities with the well characterized iodate arsenious acid and chlorite-tetrathionate autocatalytic reactions in transparent packed beads porous media. The characteristics of these porous media such as their porosity, tortuosity, and hydrodynamics dispersion are determined. In a pack of beads, the characteristic pore size and the velocity field correlation length are of the order of the bead size. In order to address these two length scales separately, we perform lattice Boltzmann numerical simulations in a stochastic porous medium, which takes into account the log-normal permeability distribution and the spatial correlation of the permeability field. In both experiments and numerical simulations, we observe stationary fronts propagating at a constant velocity with an almost constant front width. Experiments without flow in packed bead porous media with different bead sizes show that the front propagation depends on the tortuous nature of diffusion in the pore space. We observe microscopic effects when the pores are of the size of the chemical front width. We address both supportive co-current and adverse flows with respect to the direction of propagation of the chemical reaction. For supportive flows, experiments and simulations allow observation of two flow regimes. For adverse flow, we observe upstream and downstream front motion as well as static front behaviors over a wide range of flow rates. In order to understand better these observed static state fronts, flow experiments around a single obstacle were used to delineate the range of steady state behavior. A model using the “eikonal thin front limit” explains the observed steady states. © 2012 American Institute of Physics. [<http://dx.doi.org/10.1063/1.4734489>]

Autocatalytic reactions lead to fronts propagating as solitary waves with a constant velocity and invariant, flat, concentration profile resulting from a balance between reaction and diffusion. These fronts are analogous to flames in combustion and autocatalytic reactions are a kind of “cold combustion model” especially in the thin flame limit. In the presence of a hydrodynamic flow, it has already been observed and understood that such fronts while propagating at a new constant velocity, adapt their shape in order to achieve a balance between reaction diffusion and flow advection all over the front: For a viscous flow in a tube, the front is curved with zero flow at the boundary and a maximum velocity on the center line. The issue addressed here is the behavior of autocatalytic reaction fronts when the forced advection is heterogeneous in space as, for instance, inside a porous medium. The velocity field in a porous medium is characterized by the average velocity and by the standard deviation of the velocity fluctuations as well as their spatial correlations. We use both experiments in packed beads and numerical simulations which allow a control of the heterogeneities. Among the salient features observed, there exist steady, non-moving fronts over a wide range of mean flow rates in the direction contrary to the

chemical wave propagation: In this dynamical equilibrium, chemistry and flow are both at work. The front is pinned around the stagnation zones of the flow, due to the porous structure, and the front is distorted, curved in order to accommodate the local flow velocity fluctuations. To visualize the front behavior around these stagnation points, we designed an experiment of flow and chemical reaction around a single disk-obstacle. Increasing the flow rate in the adverse direction, the front could first propagate upstream, then stay static for a range of flow rate exhibiting a bottleneck shape. As the flow rate is increased, the bottleneck decreases in size. When it is too small, a pinch-off occurs and the front detaches itself from the obstacle and propagates downstream. These steady states can be explained in the thin flame limit.

I. INTRODUCTION

Interface motion and front propagation occur in many different areas, including chemical reactions,¹ population dynamics in biology (the celebrated and pioneering works of Fisher² and Kolmogorov-Petrovskii-Piskunov,³ F-KPP), and

flame propagation in combustion.⁴ Depending on the reaction kinetics, chemical reaction fronts exhibit fascinating phenomena such as Turing patterns, Belousov-Zhabotinsky (BZ) oscillations, and chaotic or solitary wave propagation.¹ Autocatalytic reaction fronts between two reacting species propagate as solitary waves at a constant velocity (V_χ) and with a stationary concentration profile⁵ of characteristic width (l_χ), described by the reaction-diffusion equation

$$\frac{\partial C}{\partial t} = D_m \Delta C + \frac{1}{\tau} f(C), \quad V_\chi \simeq \sqrt{D_m/\tau}; \quad l_\chi \simeq \sqrt{D_m \tau}, \quad (1)$$

where C is the autocatalytic concentration, τ the reaction time, D_m the molecular diffusion, and the autocatalytic concentration $f(C)$ function varies with the specific kinetics of the reaction. Fig. 1 shows such fronts for the iodate-arsenous acid (IAA)⁵ and chlorite-tetrathionate (CT) (Refs. 6 and 7) reactions. The measurement of the front velocity is often found⁸ to depend on its direction relative to the gravitational field: this effect is due to the, although tiny, density difference between reactant and product. This density difference generates buoyancy driven flows such as Rayleigh-Taylor type instabilities on horizontal fronts^{9–12} or lock-exchange gravity current in horizontal cell.^{13–17} As there is a strong retroaction between flow and buoyancy effects, it is difficult to observe the coupling between hydrodynamic velocity field and chemical waves. Therefore, the effect of forced advection on the chemical reaction, which is the effect of the space (and eventually time) dependent flow field \vec{U} on the chemical reaction deserves attention. This leads to the convection (or advection)-reaction-diffusion equation which can be written as

$$\frac{\partial C}{\partial t} + \vec{U} \cdot \nabla C = D_m \Delta C + \frac{1}{\tau} f(C). \quad (2)$$

The focus of this article is to address the coupling between the complex velocity field of a porous medium and the chemical reaction front. In contrast to flame propagation in combustion,⁴ where it has been analyzed thoroughly theoretically and experimentally, the effect of fluid flow (laminar or turbulent) on reaction fronts has not been explored in detail until recently.^{18–24} In these papers, the steady flow is unidir-

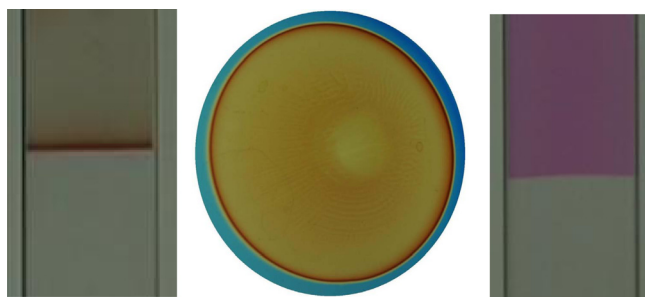


FIG. 1. From left to right IAA front stably propagating from top to bottom: the transient I_2 is detected by brown PVA. IAA front in a petri dish propagating circularly outwards: blue fresh product, yellow burnt one, and the transient PVA color. CT reaction front stably propagating from bottom to top: the reactant is purple, the product is transparent.

rectional (same direction as the chemical wave front) and is either a parabolic Poiseuille flow between two parallel solid boundaries or an unbounded spatial sinusoidal flows. The term “supportive” stands for the flow and the chemical reaction front (without flow) propagating in the same direction, and “adverse” when they are in opposite directions. More complex flows have been addressed in recent experiments in packed-bed reactors, i.e., a porous medium^{25,26} or in a cellular flow.²⁷ Using a BZ reaction in a packed-bed reactor,²⁵ it has been demonstrated that the front velocity does not follow the expected Galilean translation (Eq. (3), later on), valid under the assumption of a uniform plug-flow in such a porous medium. For supportive flow, i.e., the front travels faster than expected: a qualitative interpretation was given using a turbulent dispersion coefficient instead of the molecular diffusion. Moreover, in the case of adverse flow, the front is likely to become static (zero front velocity); a tentative explanation was made using stagnant reactive pockets. A more recent experiment²⁶ addressed the same issue in a packed bed but with a chlorite-tetrathionate (CT) chemical reaction, which confirms the possibility of obtaining a static front for adverse flow; Supportive flows are likely to follow Eq. (3) within error bars.

Even though the flow field is often assumed uniform with a mean velocity, \bar{U} , the flow field in a porous medium is more complex: for instance in a packed-bed of spherical beads, the velocity distribution²⁸ is log-normal with a correlation length of the order of the beads diameter. Therefore, it is important to work in a well characterized porous medium. For that purpose, we perform experiments with the simpler and well characterized IAA (Ref. 5) autocatalytic reaction that we have already studied in Poiseuille flow.²¹ We use a transparent packed beads porous medium for which we measure their main characteristics such as porosity, tortuosity, and hydrodynamic dispersion coefficient.²⁹ Then, we perform a series of experiments over a wide range of flow velocities and determine the main feature of the fronts. Indeed, if a pack of beads is well characterized and its characteristic lengths such as the pore size and the velocity field correlation length are both of the order of the bead size, then it is difficult to find which of these lengths is more relevant for the chemistry. To address this issue numerically, we use a lattice Boltzmann stochastic porous medium,^{30,31} which takes into account the log-normal permeability distribution and the spatial correlation of the permeability field. In order to account for the observed static state fronts, we design flow experiments around a single obstacle to delineate the range of static states; these steady states can be determined using the “eikonal thin front limit.”¹⁹

The paper is organized as follows: we first recapitulate the basic results already obtained in a simple parabolic Poiseuille velocity profile, which allows us to summarize the different regimes observed. Then, we present our investigation tools including the chemical reactions and packed beads porous media. We first analyze experiments without flow in packed beads porous media with different bead size, examining microscopic effects when the pores size is of the same order as the chemical front width. We address supportive flows in both experiments and lattice Boltzmann numerical

simulation and discuss the observed flow regimes. Adverse flow reveals static front behavior over a range of flow rates. To account for these steady states, we performed flow experiments around a single obstacle and model them using the “eikonal thin front limit.”

II. COUPLING BETWEEN PARABOLIC POISEUILLE FLOW AND AUTOCATALYTIC REACTIONS

To emphasize the key importance of the coupling between chemical reactions and hydrodynamics, we recall the main features of the theory^{19–22,24} and the experimental observations²¹ already obtained for this “simple” flow. The combined effects of flow advection, molecular diffusion, and reaction lead to a stationary front propagating at a constant velocity, V_F , with a stationary front shape depending on the underlying flow structure. Earlier, we had defined that a “stationary” front moves at constant velocity with a stationary, i.e., invariant, shape (concentration profile). A “steady” front is a special stationary front, which does not move (front velocity, $V_F = 0$). Two asymptotic regimes have been proposed: the mixing regime and the “eikonal thin front regime.” In the mixing regime, the size of the flow’s lateral extension, b , is much smaller than the chemical front width, l_χ . Therefore, molecular diffusion has enough time to transversally mix the reactants and in this regime the front velocity is simply

$$V_F = \bar{U} + V_\chi, \quad (3)$$

where \bar{U} is the average flow velocity and the velocities are algebraic quantities, positive in the direction of the chemical wave without flow (the parabolic Poiseuille profile for instance in a tube of radius R is $U(r) = U_M(1 - (r/R)^2)$, with $\bar{U} = 2U_M$). This behavior corresponds to the straight line (continuous for negative and positive \bar{U}) in Fig. 2. In this regime, we can go one step further in the analysis. If the flow velocity is slow enough that molecular diffusion can

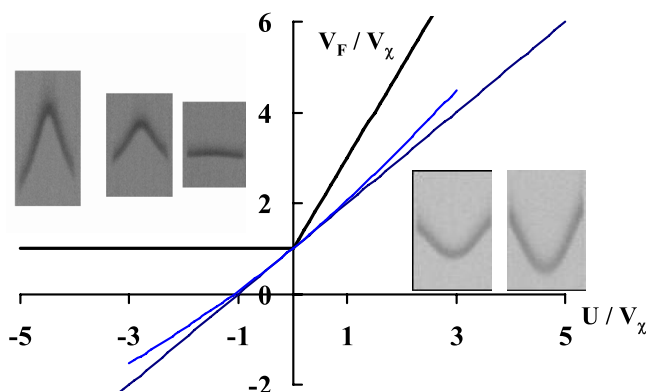


FIG. 2. Stationary chemical front in a parabolic Poiseuille flow in a rectangular Hele-Shaw cell: on the right supportive flows ($u = U/V_\chi > 0$) and on the left: adverse ($u < 0$) (the flat front corresponds to no flow). Sketch of the propagation front velocity V_F/V_χ versus the mean velocity of the Poiseuille flow, $u = U/V_\chi$; all velocities are normalized by the chemical velocity V_χ . The solid straight lines (horizontal for $u < 0$ and the more inclined for $u > 0$) correspond to the “eikonal thin front limit” ($b \gg l_\chi$). The other straight line of constant slope corresponds to the mixing regime ($b \ll l_\chi$); the curve close to it is the Taylor dispersion correction Eq. (4).

allow reactant and product to “visit” transversally, the many different flow lines, this achieves the so-called Taylor dispersion regime:³² the average concentration moves at the average speed and spreads around the mean position with a macroscopic coefficient $D_T = D_m(1 + aPe^2)$. In the latter, a is a geometrical factor and the Peclet number $Pe = \bar{U}b/D_m$ is the ratio of convective to diffusive effects. In such a regime, it was demonstrated²² that we have to use D_T instead of D_m in Eq. (2) leading to

$$\frac{V_F - \bar{U}}{V_\chi} = \frac{l_F}{l_\chi} = \sqrt{\frac{D_T}{D_m}} = \sqrt{1 + aPe^2}, \quad (4)$$

where l_F is the front width in the presence of the flow.

The eikonal regime corresponds to the contrary case where the front width is much smaller than b . It also corresponds to the thin flame regime in combustion. The front velocity depends on the flow direction relative to the chemical wave

$$\vec{V}_F \cdot \vec{n} = \vec{U} \cdot \vec{n} + V_\chi + D_m \kappa, \quad (5)$$

where \vec{U} is the local fluid velocity at the front position, \vec{n} is the local unit vector normal to the interface (oriented from product to reactant), and κ is the curvature of the interface. In this regime, the front velocity depends on the flow direction as described by Edwards¹⁹

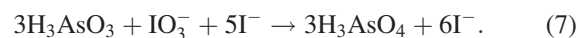
$$U > 0: V_F = U_{max} + V_\chi, \quad U < 0: V_F = V_\chi. \quad (6)$$

When the flow and the chemical reaction are in the same direction, the front velocity is sensitive to the maximum velocity of the flow, U_{max} , whereas in the opposite case, it flows upstream at its own chemical velocity, V_χ , regardless of the flow intensity.

These behaviors are sketched for a Poiseuille flow in a tube in Fig. 2.^{19–22,24} The pictures correspond to experimental observations²¹ in a rectangular Hele-Shaw cell. For intermediate values b/l_χ , the curve is in between. It is worth noting that for adverse flows (flows against the chemical wave), the overall front velocity could be either upstream or downstream depending on the flow intensity. For this situation, the front is steady ($V_F = 0$) for only a unique value of $u < 0$.

III. EXPERIMENTS

We performed experiments with the IAA autocatalytic reaction



The reaction is autocatalytic in iodide (I^-). The concentrations used are: $[\text{IO}_3^-]_0 = 7.5 \text{ mM}$ and $[\text{H}_3\text{AsO}_3]_0 = 25 \text{ mM}$. When the ratio $[\text{H}_3\text{AsO}_3]_0/[\text{IO}_3^-]_0 > 3$, the Arsenous is in excess⁵ and the front can be localized by the transient iodine generated during the reaction. The diffusion-reaction equation governing the third-order autocatalytic IAA reaction⁵ reads

$$\frac{\partial C}{\partial t} = D_m \Delta C + \frac{1}{\tau} C^2(1 - C), \quad (8)$$

where C is the concentration of the autocatalytic reactant (iodide), normalized by the initial concentration of iodate ($C = [I^-]/[IO_3^-]_0$). The balance between diffusion and reaction leads to a solitary wave of constant velocity V_χ and width l_χ ,^{1,5,9} solutions of Eq. (8) given by

$$V_\chi = \sqrt{\frac{D_m}{2\tau}}, \quad l_\chi = D_m/V_\chi. \quad (9)$$

Physically, the propagation velocity of the reaction is controlled by the combined effects of the chemical reaction rate $1/\tau$, and the diffusion of the catalyzing burnt product into the fresh solution, as $C > 0$ is a necessary condition for the reaction to begin. The above expression for V_χ reflects such combined effects. Along the same lines, the diffusive spreading of the front is mitigated by the chemical reaction, which turns the diffusing low concentration $C \simeq 0$ into $C \simeq 1$, in a characteristic time τ . This is in accordance with the expression for l_χ (Eq. (9)), which scales as the diffusion length during the time τ , namely $l_\chi \simeq \sqrt{D_m\tau}$. Instead of the usual method using starch to detect the transient iodine, we use polyvinyl alcohol (PVA) at a concentration of 6 kg/m^3 which is much more sensitive³³ and also gives a good optical contrast (Fig. 1). In addition, we add to the fluids bromocresol green *PH* sensitive dye, which gives the position of the leading edge of the reaction front: its color is blue for reactant and yellow for product. We measure $V_\chi = (11 \pm 1) \mu\text{m/s}$, from which we can infer the reaction front width, $l_\chi \simeq 100 \mu\text{m}$. Note that the uncertainty on the front velocity is not due to its measurement but to the chemical variation from one batch to the other. Note also that for the *IAA* reaction, thermal effects are negligible^{34,35} compared to the *CT* reaction.^{35,36} We have performed experiments using *CT*, for the sake of comparison with *IAA*: even if the kinetics are more complicated, we note that its chemical velocity, $V_\chi = (95 \pm 5) \mu\text{m/s}$, is ten time larger than when the typical concentrations are used.^{6,35} We follow the experimental procedure to prevent Rayleigh-Taylor instabilities and let the chemical front propagate so that the fluid left behind is in a buoyantly stable configuration, which is for *IAA* reaction downward propagation (the product is lighter than the reactant) and vice-versa for *CT* reaction.

We use two packed porous media. The first series of packed beads consists of sieved glass beads with mean diameters ranging from $d = 100$ to $1000 \mu\text{m}$ diameter and with a typical size distribution of $\pm 20\%$, porosity $\phi \simeq 40\%$, and permeability (flow resistance) $K \simeq d^2/1000$. The other “bidisperse” porous medium consists of a fifty-fifty percent mixture of two sizes of almost mono-disperse glass spheres (1.5 and 2 mm). The measured porosity of this pack is $\phi = (48 \pm 2)\%$. The beads are packed in a perspex transparent rectangular cell ($30 \times 10 \times 1 \text{ cm}^3$). The cell is held vertically along the larger extension and flows are performed along the vertical (sketch in Fig. 3). To ensure a homogeneous injection condition, a series of injectors, connected to a syringe are regularly spaced at the top of the cell and the full

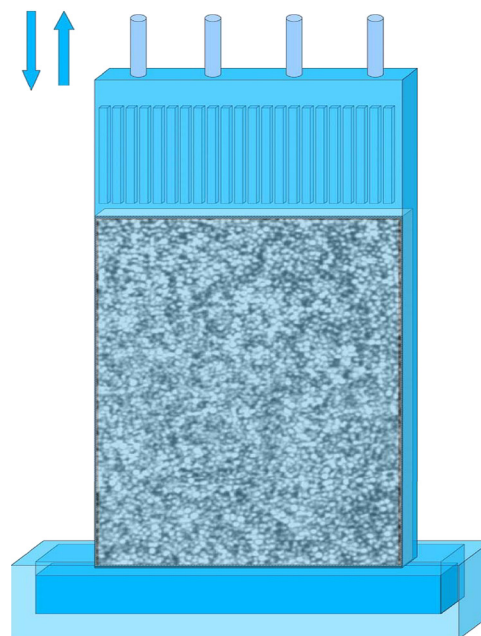


FIG. 3. Sketch of the porous medium cell. The bottom of the cell is immersed in a tank of the product. The reactant fluid is sucked or flushed through a series of injectors at the top of the cell. The cell is 30 cm high, 1 cm wide, and 1 cm thick.

bottom section bathes in a container containing the product. In this configuration, sucking from the top achieves a planar injection. An important issue to characterize the flow in porous medium is to determine its ability to mix fluids of the same density and viscosity due to the so-called hydrodynamic dispersion.^{29,37,38} for that purpose, we inject a blue-dye fluid against a transparent one at different flow rates. A 2000×1000 pixels 16 bytes (4096 gray levels) video camera is used to record the mixing front between the two fluids. The top of Fig. 4 shows a typical hydrodynamic dispersion front: the average front position travels at constant speed, ensuring that the packing is almost uniform; the fluctuation of the front position around the mean is the signature of hydrodynamic dispersion. From this data analysis, we verify the linear relationship between flow rate and average flow velocity, $Q = \phi S \bar{U}$, where Q is the volumetric flow rate, \bar{U} the mean flow velocity (first moment), and S is the cell cross-section. The front width increases as the square root of time or traveled distance: this diffusion is due to hydrodynamic dispersion whose coefficient is determined from the second moment. In Fig. 4, we present the measured hydrodynamic dispersion coefficient as a function of the mean flow rate for the large bidisperse beads pack; it should be noted that the molecular diffusion coefficient is only $D_m = 2 \cdot 10^{-9} \text{ m}^2/\text{s}$. It is worth noting that for such dispersion coefficient values, the spreading of the front is small along the cell, typically of the order of a centimeter and therefore accurate measurements are needed. The dispersion coefficient variations are linear with \bar{U} , $D = \bar{U} l_D$, leading to the dispersivity, l_D of the porous medium: $l_D = (1.8 \pm 0.1) \text{ mm}$ which is in reasonable agreement with the literature;^{29,39} it is worth noting that this value is of the order of the bead diameter (mixture of 1.5 and 2 mm beads). Note also that l_D is the correlation length of the velocity field.

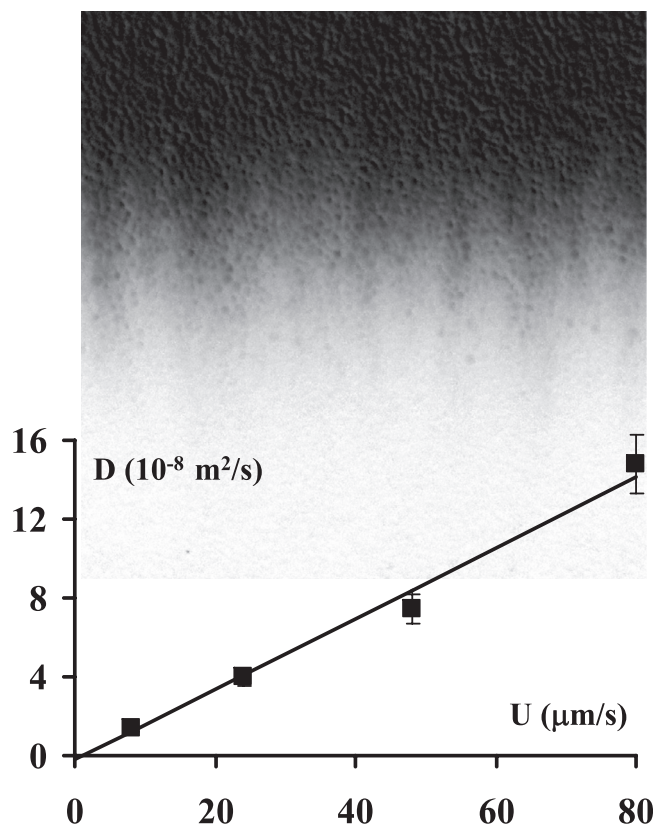


FIG. 4. Top: Typical dispersion front obtained for $\bar{U} = 24 \mu\text{m/s}$ in the 1.5–2 mm glass beads packed porous medium when dye is injected in the porous medium. The width of the picture is 10 cm. Bottom: Measurement of the hydrodynamic dispersion coefficient D of the porous medium versus the average flow velocity \bar{U} . The slope gives the dispersion length l_D .

IV. CHEMICAL FRONT PROPAGATION THROUGH THE POROUS MEDIUM WITHOUT FLOW

Using a rectangular cell without porous medium, we measure the *bulk* chemical wave-front velocity; then, we perform the experiment in the packed beads porous medium. Typical pictures of the front in the bulk (top) and inside the porous medium (bottom) are given on the left of Fig. 5. On the right of this figure is a plot of the front velocity, normalized by the chemical velocity V_F/V_χ , inside the porous media in absence of flow versus the bead size d of the packing for IAA and CT reactions. There are clearly two behaviors: for large values of d , the ratio V_F/V_χ tends to a plateau around the value $\simeq 0.8$ for both autocatalytic reactions,

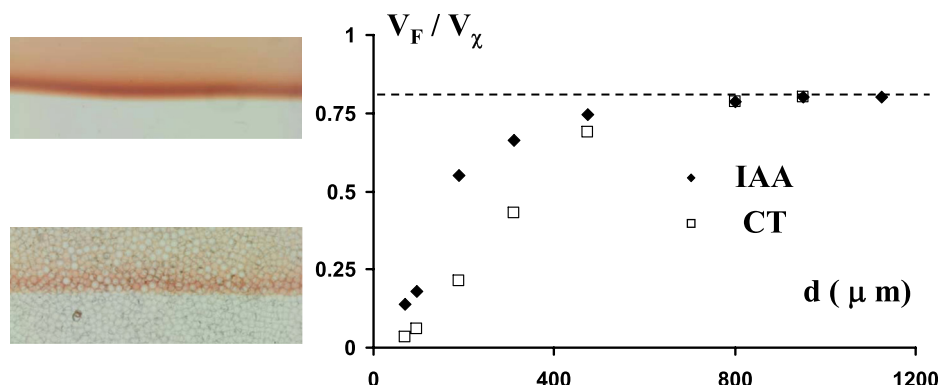


FIG. 5. Left: Pictures of IAA chemical front in bulk fluid (top) and inside a packed beads porous medium (bottom). The pictures are 8 cm wide. Right: Front velocity, normalized by the chemical velocity V_χ , versus the bead size, d of the packed beads in absence of flow for IAA and CT reaction.

whereas the ratio decreases drastically down to almost zero as the bead size decreases.

The plateau can be easily understood if one recalls that the multi-connected porous medium has got not only a porosity but also a tortuosity, α : the tortuosity⁴⁰ is a geometrical factor accounting for the loss in efficiency of diffusion phenomena, compared to the bulk, due to the solid skeleton of the porous medium. As a result, the molecular diffusion inside the porous medium, D_{mPM} , is reduced by this factor: $D_{mPM} = D_m/\alpha$. Therefore, using Eq. (9), it is straightforward to account for the decrease of the front velocity inside the porous medium

$$V_{\chi PM} = \sqrt{\frac{D_{mPM}}{2\tau}} = \frac{V_\chi}{\sqrt{\alpha}}. \quad (10)$$

From our measurements, the tortuosity is $\alpha = 1.7 \pm 0.2$ in agreement with the values found in the literature.^{29,39}

The drastic decrease to zero appears at a value around $500 \mu\text{m}$ downwards and it appears earlier for the CT reaction than for the IAA one: this effect might be understood as a microscopic effect observable when the pore size is of the order of the chemical width l_χ . The drastic decrease appears earlier for CT reaction than for IAA as the CT chemical width is larger³⁵ than that of the latter.

To confirm this hypothesis, we perform experiments on a corner film flow left by an air bubble in a square capillary of edge a , shown⁴¹ in Fig. 6; this topology is reminiscent of the pore structure inside the packed beads porous medium. The pictures in Fig. 6 show the front before and after the air bubble and after entering the bubble zone. The dynamics are such that first the front propagates at its constant velocity V_χ , when it reaches the bubble, it enters the constriction at almost the same speed; then, it takes a long time for it to cross the diverging opening constriction. A more quantitative measurement can be obtained by defining an effective velocity as the air bubble length divided by the waiting time to get across the bubble: this velocity is plotted in Fig. 6 versus the capillary tube edge a . The sketch⁴¹ suggests that the typical radius of corner flow is one order of magnitude smaller than a , leading to a value for intense velocity reduction, $800/10 = 80 \mu\text{m}$, which is roughly the chemical front width l_χ . The physical interpretation of the latter is that in the divergence of the constriction the front is constrained to the curve (radius of curvature R) and hence there is not enough material to sustain front

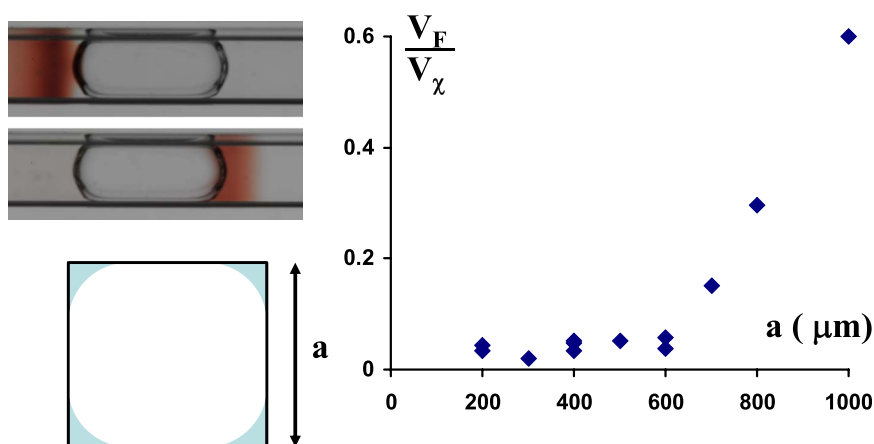


FIG. 6. Left: pictures of the chemical wave propagation across the corner film left by an air bubble quenches in square capillary tube of edge a . Right: Front velocity, normalized by the chemical velocity V_χ , versus the square capillary tube edge a . The sketch shown in blue corresponds the corner liquid space left by the air bubble.⁴¹

reaction: a semi-quantitative argument can be found from the eikonal Eq. (7): in the absence of flow, the velocity of the front, $V_\chi + D_m \kappa$, may vanish for a curvature of the front κ , negative and of the order of $|\kappa| \simeq V_\chi / D_m = 1/l_\chi$, which is $R \simeq l_\chi$. This might be the picture that we can use to figure out the behavior of the front inside the glass beads packs.

V. CHEMICAL FRONT PROPAGATION FOR SUPPORTIVE FLOW

A. Experiments in the bidisperse beads pack

We perform experiments corresponding to supportive flow in the bidisperse 1.5–2 mm beads pack for which we have measured the hydrodynamic dispersion coefficient (Fig. 4). As defined earlier, supportive flows correspond to the case where the flow and the chemical reaction front (without flow) are in the same direction. In order to get results to compare with analogous experiments with different chemical reactions,^{25,26} we cover a wide range of flow velocities up to $\bar{U} \sim 40 V_\chi$. For all the experiments, the front achieved a stationary state with a constant front velocity V_F and a constant width; it should be noted that even if the front width is constant it fluctuates with time. The left plot of Fig. 7 shows a typical stationary front obtained for $u = \bar{U}/V_\chi = 10.2$. The plot on the right shows that the dependence between V_F/V_χ and $u = \bar{U}/V_\chi$

$$V_F = V_{\chi PM} + \beta \bar{U} \quad (11)$$

with $\beta = 1.20 \pm 0.05$. This does not agree with the mixing law Eq. (3). Moreover, the wide range covered allows us to test whether Eq. (4) is relevant to our data. In that case,²² the diffusion coefficient D_T has to be replaced by the hydrodynamic dispersion coefficient, $D = \bar{U} l_D + D_m/\alpha$: this is the curved line in the inset of Fig. 7, which shows the comparison with our data taking into account our measurements of the hydrodynamic dispersion Fig. 4, in the same sample in the same range of flow rates. Our data falls between the straight line mixing regime Eqs. (3) and (4). This is not really surprising as the typical size of our beads (1.5–2 mm) and the correlation length of the velocity field $l_D = 1.8$ mm are both much larger than the chemical width of our front ($l_\chi \sim 100 \mu\text{m}$) and, therefore, the system is out of the mixing regime.²² This however may be not the case in Ref. 25 where the beads size was smaller. As the front velocity Eq. (11) is fairly linear over a wide range of velocities and as our experiment is closer to the eikonal regime, it is likely that Eq. (11) can be understood using the eikonal equation (Eq. (7)) in which case the chemical front attains a maximum velocity $U_{max} = \beta \bar{U}$. This would mean that this velocity is a kind of correlated maximum velocity across the porous medium. This point is further explored in the framework of percolation-type correlated paths through the porous structure.⁴²

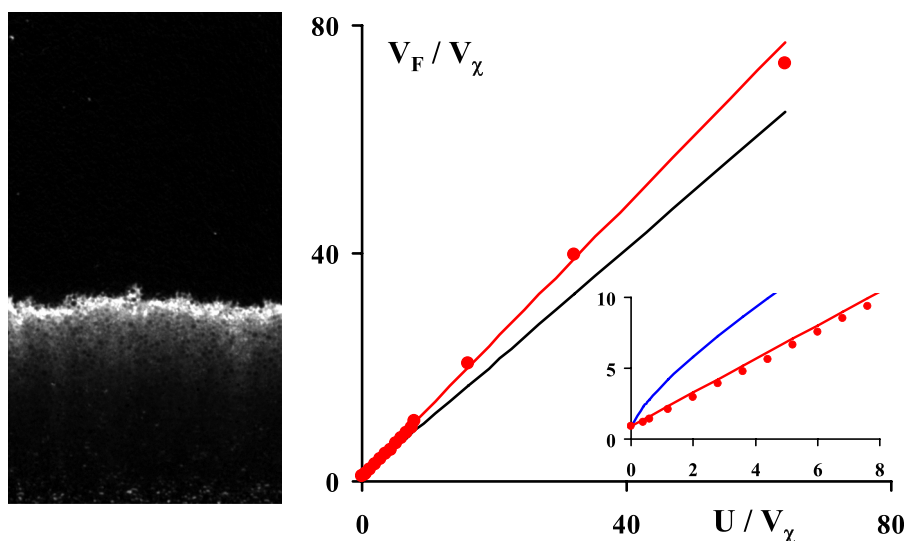


FIG. 7. Supportive flow. Left: stationary front obtained for $u = \bar{U}/V_\chi = 10.2$ in the 1.5–2 mm beads pack; the picture is 10 cm wide. Right: front velocity V_F/V_χ versus the mean flow velocity in the porous medium, \bar{U}/V_χ . The straight line of slope 1.20 through the data is the best fit of the linear dependency of the front velocity with the flow rate. The black straight line is the plug flow, Galilean translation, model Eq. (3). The inset corresponds to a close-up of the same data, with the comparison with the Taylor model Eq. (4) (curve line) using the measured dispersion coefficient Fig. 4.

B. Numerical simulations in stochastic porous medium

Glass beads packing has a correlation length of the order of the pore/bead size, but more realistic porous media might be more heterogeneous. As shown above, the correlation length of the velocity field has a strong influence on the front velocity. Permeability heterogeneities in porous media are a well-recognized factor in many practical applications, in fields such as hydrology, petroleum, and environmental engineering. Heterogeneities create preferential and non-preferential flow paths, which greatly enhance the spreading of pollutants, or conversely lead to the bypassing of targeted zones containing organic liquids. The influence of heterogeneity on the field-scale dispersion of passive tracers has been studied extensively. One possible approach is based on the stochastic continuum,^{43–45} which is based on Darcy’s law where the permeability field’s spatial distribution is generated using a given probability and correlation function. This approach provides a significant understanding of the macro-scale dispersion as a function of the statistical properties of the permeability field. In the present work, following this approach, we generate a porous medium stochastically as described in Ref. 46, using a log-normal distribution with an exponential correlation function (see Figure 8)

$$R_{ff}(\vec{\zeta}) = E(f'(\vec{r})f'(\vec{r} + \vec{\zeta})) = \sigma_f^2 \exp\left(-\frac{|\vec{\zeta}|}{\lambda}\right), \quad (12)$$

where λ is the correlation length. The log-normal distribution is characterized by its mean, $f_0 = \log(K)$ and its standard deviation (root-mean-square (RMS)), $\sigma^2 = (\log(K) - f_0)$. For such a permeability field, the asymptotic macro-dispersion coefficient of the corresponding porous medium is given by

$$D_{macro} = \sigma^2 \lambda \bar{U}, \quad (13)$$

where \bar{U} is the average flow velocity through the porous medium. It is worth noting that in such a medium, the

hydrodynamic dispersion depends both on the amplitude of the heterogeneities (σ) and the correlation length λ . One should also note that the use of another correlation function would modify this expression by changing the prefactor.

When the permeability fluctuations are over small distances, Darcy’s law may not adequately describe the conservation of momentum. It is indeed well known that Darcy’s law breaks down near sharp discontinuities in permeability (for example, across different permeability blocks or at the free liquid-porous medium interface). To connect the resulting discontinuities, an additional diffusion momentum term (the Brinkman correction^{30,47,48}) is typically added to Darcy’s equation, leading to

$$\vec{\nabla} P = -\frac{\mu}{K} \vec{V} + \mu_e \Delta \vec{V}, \quad (14)$$

where μ_e is an effective viscosity.

As described in Talon *et al.*,⁴⁶ we solve Darcy-Brinkmann Eq. (14) and the convection-reaction-diffusion Eq. (2) using a Lattice-Boltzmann based scheme. In summary, those schemes are based on the discretization of the Boltzmann equation that describes the evolution of the velocity probability distribution function of the fluid particles (e.g., Refs. 49 and 50). The most standard version (Bathnagar-Gross-Krook (BGK)) solves the Navier-Stokes (or Stokes) equation and a Darcy term can be introduced by adding an extra momentum source (see Refs. 51–53), which leads to the general form of the Brinkman equation (Eq. (14)). In the present work, we have set $\mu_e = \mu$, for the sake of simplicity.

Using the above stochastic porous medium Fig. 8, we include the IAA chemical reaction as described in our previous work.^{11,22,24} After an initial transient, the fronts propagate at constant velocity V_F and stationary width l_F . Fig. 9 depicts a series of fronts at the same velocity and correlation length for different amplitudes of heterogeneities σ (top) and a series of fronts (bottom) for different velocities \bar{U} keeping the other parameters constant. On the right, we plot $(V_F - \bar{U})/V_\chi)^2 - 1$ versus \bar{U} (bottom) and versus σ^2 (top); obviously, these two dependences are linear. One should mention that the

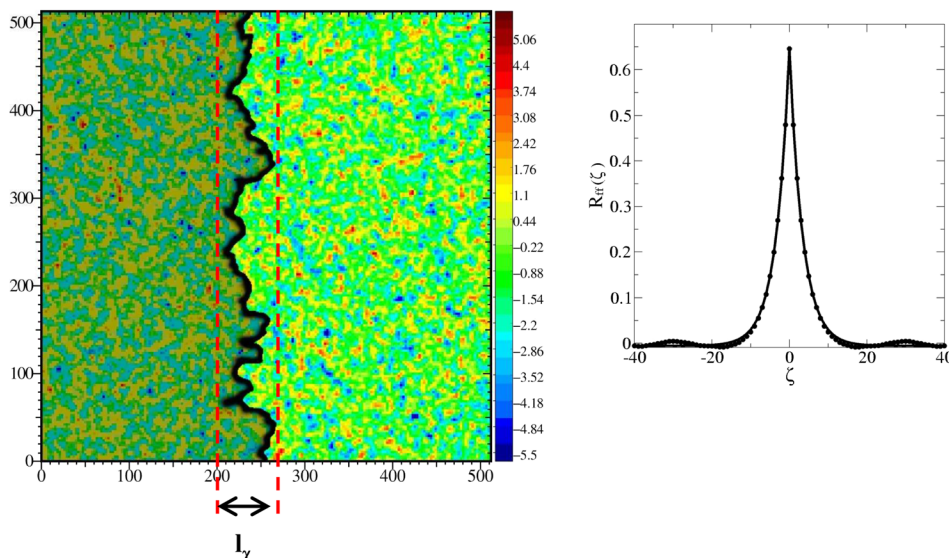


FIG. 8. Stochastic porous medium. Left: Color map of the permeability field of one realization of a porous medium, characterized by a log-normal isotropic distribution of mean -1 , RMS $\sigma = 0.8$, and correlation length $\lambda = 3.4$ in lattice units. The color map on the right corresponds to the local value of the permeability. The black line corresponds to the chemical wave front inside the porous medium for a relative velocity $\bar{U}/V_\chi = 2$ and a mean standard deviation of the permeability distribution $\sigma = 0.5$. Right: Measured covariance function of the log-normal isotropic distribution of the left permeability field. The value of λ was obtained by an exponential fit (line) using Eq. (12).

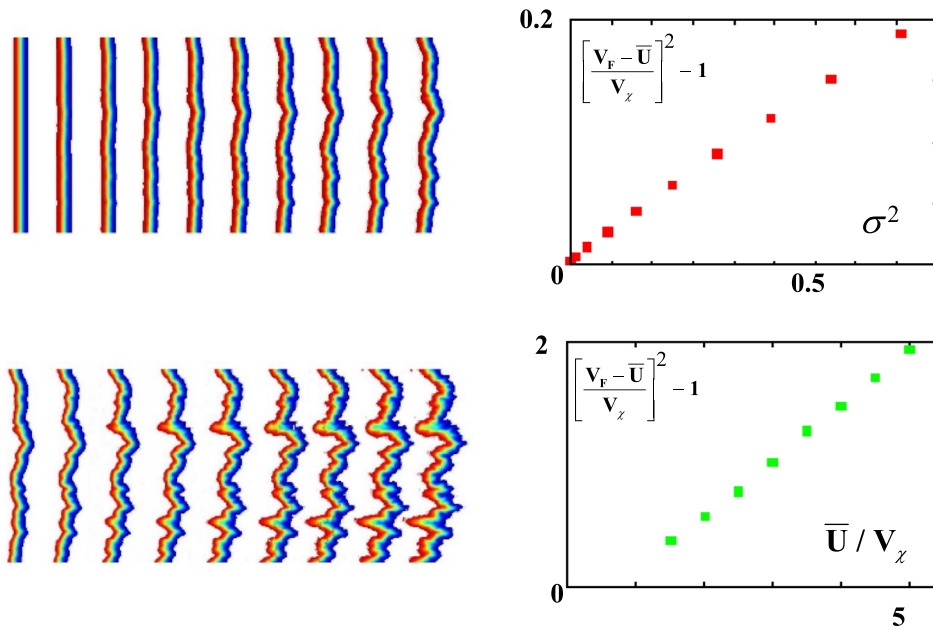


FIG. 9. Numerical simulations. Top left: series of fronts at a given velocity $\bar{U}/V_\chi = 1$ and correlation length $\lambda/l_\chi = 1$ for different size distributions σ from 0 to 0.9. Bottom left: series of fronts at a given $\sigma = 0.9$ for different velocity \bar{U}/V_χ from 1 to 5. Right: Plot of $(V_F - \bar{U})/V_\chi)^2 - 1$ versus the square of the size distribution, σ^2 (top) and versus the normalized flow velocity \bar{U}/V_χ (bottom).

dependence on λ is also linear (not presented here). The same relations are also observed for the relative front width $(l_F/l_\chi)^2 - 1$. By changing the different parameters, as shown by Fig. 10, our simulations yield to the scaling law

$$\left(\frac{V_F - \bar{U}}{V_\chi}\right)^2 - 1 \simeq \sigma^2 \frac{\lambda \bar{U}}{l_\chi V_\chi} = \frac{D_{macro}}{D_m}. \quad (15)$$

This result can be understood by using the same approach as for Eq. (4), where the D_T needs to be replaced by $D_m + D_{macro} = D_m + \sigma^2 \lambda \bar{U}$. We should however mention that although the scaling law is correct, this argument does not give the correct prefactor. Compared to the experiments, the numerical simulations are performed with both small correlation length compared to the chemical length $\lambda/l_\chi \leq 2$ and rather small flow velocity $\bar{U}/V_\chi \leq 5$, so that the diffusive Taylor like regime can be observed in agreement with Leconte *et al.*²² The above experiments in large bead packs

correspond to the contrary regime ($l_D/l_\chi \geq 10$), hence closer to the “eikonal thin front” regime where the system is more sensitive to large velocities. The key point of these results imply that in Eq. (15), the front velocity and width chosen by the system also give information on the underlying flow properties of the porous medium without chemistry, namely its hydrodynamic dispersion D_{macro} ; this effect has also been observed in, although very different context, chemical lock-exchange gravity current.¹⁶

VI. CHEMICAL FRONT PROPAGATION FOR ADVERSE FLOW

As implicitly assumed above, we choose the chemical reaction velocity V_χ as the reference velocity direction, therefore $\bar{U} > 0$ corresponds to supportive, co-current flow and $\bar{U} < 0$ to adverse flow. The variation of V_F/V_χ versus $u = \bar{U}/V_\chi$ is shown at the bottom of Fig. 11.

If the co-current, supportive flow follows the expected behavior of a front moving in the direction of both the chemistry and the average flow ($U > 0, V_F > 0$), then for adverse flow, the situation is more complex and richer than the former. The front velocity V_F could be either positive or negative relative to the chemical velocity

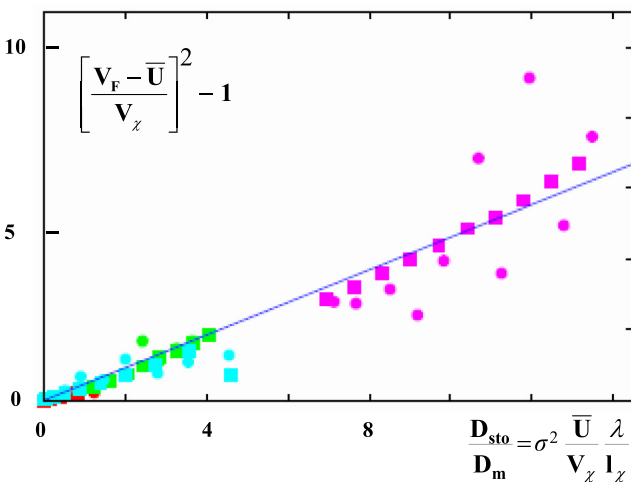


FIG. 10. Numerical simulations. Plot of $(V_F - \bar{U})/V_\chi)^2 - 1$ versus the variable $\sigma^2 \frac{\lambda \bar{U}}{l_\chi V_\chi}$ (see Eq. (15)) for different series of variation of $\sigma, \bar{U}/V_\chi$, or λ/l_χ and different statistical porous medium.

- (1) For small adverse flow rates, the fronts could still propagate in the direction of the chemical wave ($V_F > 0$) and, therefore, propagate upstream opposite to the hydrodynamic flow; the front velocity variations are in continuation of the supportive values down to zero. This regime is observed for $-1 \leq u \leq 0$. In this situation, the chemical front propagation overcomes the imposed flow.
- (2) The plateau ($-3.2 \leq u \leq -1$) corresponds to a static front ($V_F = 0$). It is worth noting that for a Hele-Shaw cell Poiseuille flow,²¹ steadiness is only observed for a single u value (Fig. 2). Here, the fluctuations of the velocity field around the mean leads to this wide plateau; such static fronts have already been reported in

packed-bed reactors^{25,26} but for very different chemistries, a tentative explanation was provided using stagnant reactive pockets. A more recent experiment²⁶ addressed the same issue in a packed bed but with a CT chemical reaction, which confirmed the possibility of steady fronts in adverse flow. It should be emphasized that if the front is steady, the spatially fluctuating flow and the chemistry are both at work, but in opposite directions such that all over the front an equilibrium between the two effects is achieved. From Eq. (7), this could be achieved for different flow velocities provided the angle between the front and the flow varies. Note that starting from different initial conditions can lead to different final positions of the steady front in the sample.

- (3) For $u \leq -3.2$, the front starts to move again at constant (but negative) velocity and, therefore, in the downstream flow direction. Its velocity is almost linear with U , but as opposed to supportive fronts the corresponding selected flow velocities are smaller than the mean, in agreement with¹⁹ as sketched in Fig. 2.

To summarize on the different regimes observed: Compared to a non fluctuating invariant flow field along the flow direction (Figs. 2 and 11), the overall trend of the front velocity variations are comparable but with a wide static front plateau

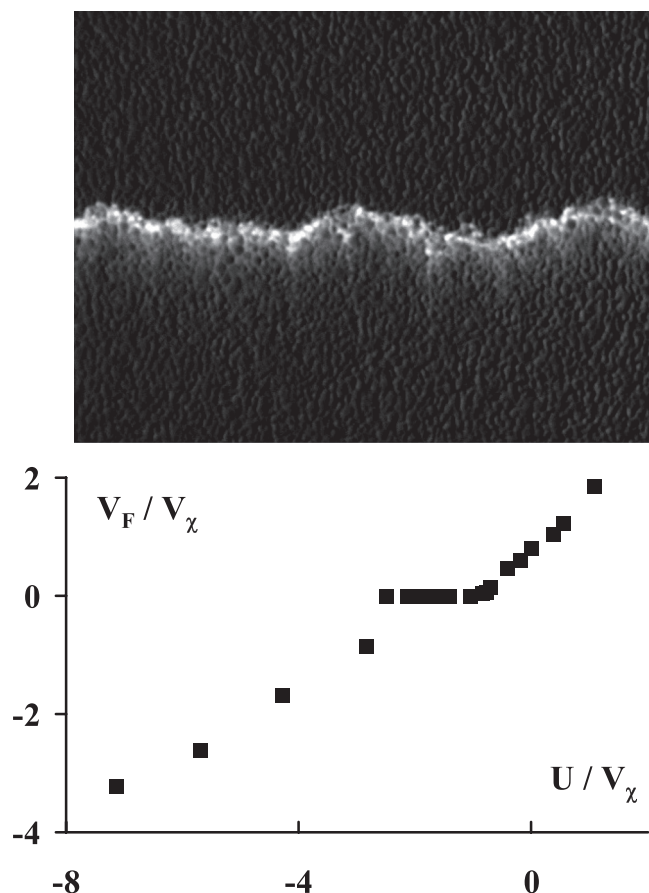


FIG. 11. Top picture (width 10 cm) of the front for $\bar{U}/V_\chi = -0.5$, which propagates upstream ($V_F > 0$). Bottom: Normalized front velocity, V_F/V_χ , versus average flow velocity \bar{U}/V_χ for adverse flow inside the 1.5–2 mm beads pack.

for adverse flows. The possibility of such a steady state is addressed in Sec. VII, well designed and known flow fields. The images of Figs. 7 and 11 show a front structure which obviously present different roughness depending on the flow regimes; this question is addressed in Ref. 42 and 54.

VII. STEADY FRONTS IN FLOW PAST A DISK

The key issue raised in the former section is the possibility of steady fronts ($V_F = 0$) over a range of adverse flow velocities. Indeed, keeping in mind that the grains of a porous medium are a kind of solid obstacles in a hydrodynamic flow, we decide for the sake of visualization to address this issue in a quasi 2D velocity field of a single disk obstacle.

For that purpose, we use a 250 μm thin Hele-Shaw cell (two parallel plates separated by a 250 μm gap). The obstacle is a solid disk of radius 1 cm (Fig. 12). Its size is 40 times larger than the gap of the cell, leading to a 2D Hele-Shaw cell flow.⁵⁵ The flow of the fresh reactant is performed at a constant velocity U_0 from left to right. In the absence of flow, the chemical front propagates from right to left.

- (1) For $u = U_0/V_\chi > -1$, the front propagates in the chemical wave direction as expected that is upstream.
- (2) For $-5 < u < -1$, the front achieves a steady state shape ($V_F = 0$): the 3 images on the left of Fig. 12 are some examples.
- (3) For $u < -5$, the flow is large enough to overcome chemical reaction and the front detaches from the disk obstacle and propagates downstream ($V_F < 0$): the 3 images on the right in Fig. 12 show the dynamics of such a detachment (time increases from top to bottom).

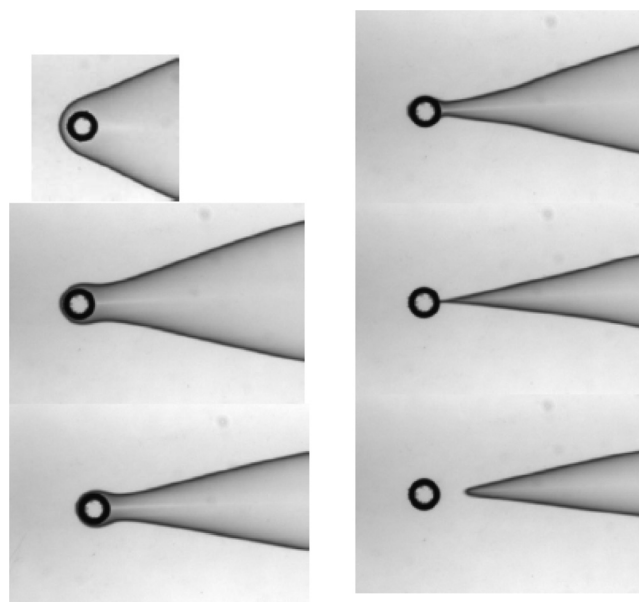


FIG. 12. Chemical front in a flow around an obstacle; the flow is from left to right. The injection of the fresh reactant produces a flow at constant velocity U_0 in a 250 μm thin Hele-Shaw cell; the solid disk obstacle is a cylinder of diameter 1 cm. The chemical front in the absence of flow would propagate from right to left. Left pictures: from top to bottom, steady fronts around the same disk for $U_0/V_\chi = -1.5, -3$, and -5 . Right: 3 pictures of time sequence of detachment from the obstacle at a larger velocity $U_0/V_\chi \approx -9$ (time increases from top to bottom).

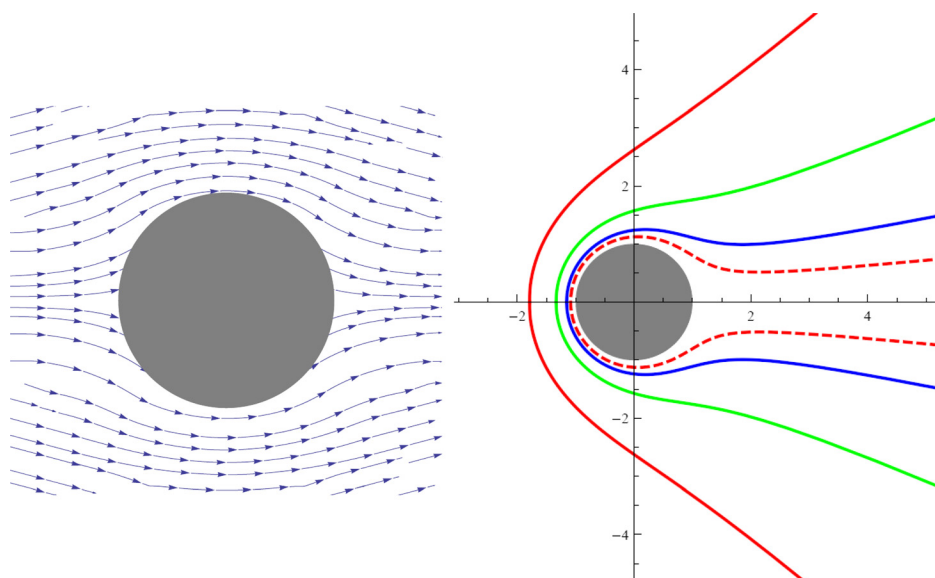


FIG. 13. Left: Velocity field around a disk, placed in a uniform adverse flow U_0 . The flow is from left to right. In the absence of flow, the chemical front propagates from right to left. Right: Steady fronts around the disk obtained from integration of Eq. (7), with $V_F = 0$, for $U_0/V_\chi = -1.5, -2.5, -5$, and -10 .

Therefore, this simple experiment clearly shows that a single obstacle is able to reproduce the features observed in the porous medium in an adverse flow, namely upstream fronts, a range of steady fronts, and downstream ones.

In order to account for the shape of these steady fronts, we theoretically address the issue of the “eikonal thin front limit” given by Eq. (7). The flow field in the Hele-Shaw around the disk is well known: at leading order, it is the potential flow around a disk. Its expression in polar coordinate (r, θ) is⁵⁶

$$v_r = U_0 \left(1 - \frac{R^2}{r^2} \right) \cos \theta; \quad v_\theta = -U_0 \left(1 + \frac{R^2}{r^2} \right) \sin \theta, \quad (16)$$

where R is the disk radius. Note that for a viscous flow, the velocity must be zero on the boundary, therefore, there are boundary layer type corrections which extend over a typical size of the order of the thin gap. The corresponding velocity field is plotted in the left of Fig. 13. Using the analytical expression and including the boundary layer effect, we integrated the eikonal equation (Eq. (7)) for steady state ($V_F = 0$). For that purpose, we calculate the asymptotics in the vicinity of $\theta = \pi$ and integrate from the corresponding point. The right plot in Fig. 13 shows four such steady fronts. Compared to the experiments shown on the left of Fig. 12, we obtained very similar shapes to the ones from the model Fig. 13. As $|U_0/V_\chi|$ increases, the front shape becomes thinner exhibiting a clear bottleneck downstream (right of the disk). The understanding of the detachment observed in the experiment (right in Fig. 12) is likely because increasing $|U_0/V_\chi|$ leads to a thinning of the bottleneck. In the “eikonal thin front limit,” this bottleneck can reduce down to zero without problem. A chemical front has a finite extension l_χ , therefore when the bottleneck becomes of the order of the chemical width, this can lead to a pinch-off of the two branches of the front, followed by detachment.

VIII. CONCLUSIONS

In this paper, we addressed experimentally and by numerical simulations the issue of the chemico-hydrodynamic

coupling between forced advection in porous media and self-sustained chemical waves. First, we analyzed experiments without flow in packed beads porous media with different bead sizes, discovering the influence of the tortuosity and microscopic effects when the pores are of the size of the chemical front width. For supportive flows, experiments and simulations allow observation of two flow regimes. For adverse flow, we observe upstream and downstream fronts as well as static front behavior over a wide range of flow rates. In order to investigate these observed steady state fronts, flow experiments around a single obstacle were used to delineate the range of steady state, which can be modeled using the “eikonal thin front limit.”

ACKNOWLEDGMENTS

It is a pleasure to acknowledge the contribution of M. Böckmann, M. Leconte, I. Bou Malham, and N. Jarrige and stimulating discussions inside the ESA Topical Team “Chemo Hydrodynamic Pattern Formation” with Bordeaux, Brussels, Dresden, Magdeburg, Szeged, and Toulouse groups. The research was partly supported by IDRIS (project 034052), CNES No 793/CNES/00/8368, ESA (No AO-99-083), Agence Nationale de la Recherche (ANR) “Coliner,” Réseaux de Thématiques de Recherches Avancées “Triangle de la physique” and by the Initial Training Network (ITN) “Multiflow.” S.S. was supported by ITN “Multiflow,” S.S. by a CNRS Ph.D. Grant and D.S. partly by Institut Universitaire de France. All these sources of support are gratefully acknowledged.

¹S. K. Scott, *Oscillations, Waves, and Chaos in Chemical Kinetics*, Physical Vol. 18 (Oxford University Press, 2004).

²R. Fisher, *Annu. Eugen.* **7**, 355 (1937).

³A. Kolmogorov, I. Petrovsky, and N. Piscounoff, *Bull. Univ. Moscow, Ser. Int. A* **1** (1937).

⁴Y. Zeldovich and D. Frank-Kamenetskii, *Zh. Fiz. Khim* **12**, 100 (1938).

⁵A. Hanna, A. Saul, and K. Showalter, *J. Am. Chem. Soc.* **104**, 3838 (1982).

⁶A. Toth, D. Horvath, and A. Siska, *J. Chem. Soc.* **93**, 73 (1997).

⁷J. D. Horváth, T. Bánsági, and Á. Tóth, *J. Chem. Phys.* **117**, 4399 (2002).

⁸J. A. Pojman and I. R. Epstein, *J. Phys. Chem.* **94**, 4966 (1990).

- ⁹M. Böckmann and S. C. Müller, *Phys. Rev. Lett.* **85**, 2506 (2000).
- ¹⁰A. De Wit, *Phys. Rev. Lett.* **87**, 054502 (2001).
- ¹¹J. Martin, N. Rakotomalala, D. Salin, and M. Böckmann, *Phys. Rev. E* **65**, 051605 (2002).
- ¹²J. Martin, N. Rakotomalala, and D. Salin, *Phys. Fluids* **14**, 902 (2002).
- ¹³L. Rongye, N. Goyal, E. Meiburg, and A. De Wit, *J. Chem. Phys.* **127**, 114710 (2007).
- ¹⁴G. Schuszter, T. Toth, D. Horvath, and A. Toth, *Phys. Rev. E* **79**, 016216 (2009).
- ¹⁵J. Martin, N. Rakotomalala, L. Talon, and D. Salin, *J. Fluid Mech.* **673**, 132 (2011).
- ¹⁶I. Bou Malham, N. Jarrige, J. Martin, N. Rakotomalala, L. Talon, and D. Salin, *J. Chem. Phys.* **133**, 244505 (2010).
- ¹⁷N. Jarrige, I. Bou Malham, J. Martin, N. Rakotomalala, D. Salin, and L. Talon, *Phys. Rev. E* **81**, 066311 (2010).
- ¹⁸B. Audoly, H. Berestycki, and Y. Pomeau, *C. R. Acad. Sci. Paris, Ser. II B* **328**, 255 (2000).
- ¹⁹B. F. Edwards, *Phys. Rev. Lett.* **89**, 104501 (2002).
- ²⁰B. F. Edwards, *Chaos: Interdis. J. Nonlinear Sci.* **16**, 043106 (2006).
- ²¹M. Leconte, J. Martin, N. Rakotomalala, and D. Salin, *Phys. Rev. Lett.* **90**, 128302 (2003).
- ²²M. Leconte, J. Martin, N. Rakotomalala, and D. Salin, *J. Chem. Phys.* **120**, 7314 (2004).
- ²³D. A. Vasquez, *Phys. Rev. E* **76**, 056308 (2007).
- ²⁴M. Leconte, N. Jarrige, J. Martin, N. Rakotomalala, D. Salin, and L. Talon, *Phys. Fluids* **20**, 057102 (2008).
- ²⁵M. Kaern and M. Menzinger, *J. Phys. Chem. B* **106**, 3751 (2002).
- ²⁶I. V. Kopyug, V. V. Zhivonitko, and R. Z. Sagdeev, *J. Phys. Chem. B* **112**, 1170 (2008).
- ²⁷M. E. Schwartz and T. H. Solomon, *Phys. Rev. Lett.* **100**, 028302 (2008).
- ²⁸L. Lebon, L. Oger, J. Leblond, J. Hulin, N. Marty, and L. Schwarz, *Phys. Fluids* **8**, 293 (1996).
- ²⁹J. Bacri, N. Rakotomalala, and D. Salin, *Phys. Rev. Lett.* **58**, 2035 (1987).
- ³⁰L. Talon, J. Martin, N. Rakotomalala, D. Salin, and Y. Yortsos, *Water Resour. Res.* **39**, 1135 (2003).
- ³¹L. Talon, J. Martin, N. Rakotomalala, and D. Salin, *Phys. Fluids* **16**, 4408 (2004).
- ³²G. I. Taylor, *Proc. R. Soc. London, Ser. A* **219**, 186 (1953).
- ³³T. Yoshinaga, M. Tsuschida, Y. Toyose, H. Hiratsuka, and M. Yamaye, *Anal. Sci.* **20**, 549 (2004).
- ³⁴J. A. Pojman, I. R. Epstein, T. J. McManus, and K. Showalter, *J. Phys. Chem.* **95**, 1299 (1991).
- ³⁵J. Martin, N. Rakotomalala, L. Talon, and D. Salin, *Phys. Rev. E* **80**, 055101 (2009).
- ³⁶P. Grosfils, F. Dubois, C. Yourassowsky, and A. De Wit, *Phys. Rev. E* **79** (2009).
- ³⁷J. Bacri, N. Rakotomalala, and D. Salin, *Phys. Fluids A: Fluid Dyn.* **2**, 674 (1990).
- ³⁸J. Martin, N. Rakotomalala, and D. Salin, *Phys. Rev. Lett.* **74**, 1347 (1995).
- ³⁹J.-P. Hulin and D. Salin, in *Disorder and Mixing*, edited by J. N. E. Guyon and Y. Pomeau (Kluwer Academic Publishers, 1988), chap. 5.
- ⁴⁰J. Bear, *Dynamics of Fluids in Porous Media* (Elsevier, New York, 1988).
- ⁴¹H. Wong, S. Morris, and C. Radke, *J. Colloid Interface Sci.* **148**, 317 (1992).
- ⁴²S. Saha, S. Atis, H. Auradou, D. Salin, and L. Talon (submitted).
- ⁴³G. Matheron, *Éléments Pour une Théorie des Milieux Poreux* (Masson Paris, 1967).
- ⁴⁴G. Dagan, *Water Resour. Res.* **18**, 835 (1982).
- ⁴⁵L. Gelhar and C. Axness, *Water Resour. Res.* **19**, 161 (1983).
- ⁴⁶L. Talon, J. Martin, N. Rakotomalala, D. Salin, and Y. Yortsos, *Phys. Rev. E* **69**, 066318 (2004).
- ⁴⁷H. Brinkman, *Appl. Sci. Res. A* **1**, 27 (1947).
- ⁴⁸J. Zeng, Y. C. Yortsos, and D. Salin, *Phys. Fluids* **15**, 3829 (2003).
- ⁴⁹Y. Qian, D. D'Humières, and P. Lallemand, *Europhys. Lett.* **17**, 479 (1992).
- ⁵⁰S. Chen and G. Doolen, *Annu. Rev. Fluid Mech.* **30**, 329 (1998).
- ⁵¹N. Marty, D. Bentz, and E. J. Garboczi, *Phys. Fluids* **6**, 1434 (1994).
- ⁵²N. S. Marty, *Phys. Fluids* **13**, 1807 (2001).
- ⁵³I. Ginzburg, *Phys. Rev. E* **77**, 066704 (2008).
- ⁵⁴S. Atis, S. Saha, H. Auradou, L. Talon, and D. Salin (submitted).
- ⁵⁵H. J. S. Hele-Shaw, *Nature (London)* **58**, 34 (1898).
- ⁵⁶H. Lamb, *Hydrodynamics*, 6th ed. (Cambridge University Press, 1932).